Prediction of the daily spatial variation of stem water potential in cherry orchards using weather and Sentinel-2 data

Francisco Zambrano[a,b], Abel Herrera[a], Mauricio Olguín[c,d], Miro Miranda[e],Jesica Garrido[a], Andrea Miyasaka Almeida[c,d]

[a]Hemera Centro de Observación de la Tierra, Facultad de Ciencias, Escuela de Ingeniería en Medio Ambiente y Sustentabilidad, Universidad Mayor, Santiago, Chile.

[b]Observatorio de Sequía para la Agricultura y la Biodiversidad de Chile (ODES), Universidad Mayor, Santiago, Chile.

[c]Centro de Genómica y Bioinformática, Facultad de Ciencias, Ingeniería y Tecnología, Universidad Mayor, Santiago 8580745, Chile.

[d]Escuela de Agronomía, Facultad de Ciencias, Ingeniería y Tecnología, Universidad Mayor, Santiago 8580745, Chile.

[e]German Research Center for Artificial Intelligence (DFKI) Kaiserslautern, Germany

Corresponding author. Email: francisco.zambrano@umayor.cl

This paper is a non-peer reviewed preprint submitted to EarthArXiv.

Abstract

Irrigation management is critical for orchard production and plays a key role when there is water scarcity. Climate change is changing global precipitation and temperature patterns, causing more frequent and intense drought periods in some parts of the world. Thus, there is a challenge to optimizing water use efficiency. The common practice for irrigation management is to apply the water lost by evapotranspiration. However, we could manage the irrigation by monitoring the plant's water status by measuring the stem water potential (Ψ_s), which is currently costly and time-consuming. Here, we predicted the daily spatial variation of Ψ_s. In the central part of Chile, during two seasons (2022-2023 and 2023-2024, between October and April), we measured Ψ_s in two orchards planted with sweet cherry tree variety Regina, and we monitored 30 trees weekly and biweekly. To predict the Ψ_s, we used the random forest (RF), extreme gradient boosting (XGBoost), and support vector machine (SVM) models. We selected vapor pressure deficit (VPD), reference evapotranspiration (ET0), relative humidity, and temperature as weather predictors. Spectral vegetation indices (VIs) and biophysical parameters were derived from Sentinel-2. We compared two split schemes for training and testing, one with complete randomness (*rnd_split*) and the other with daytime independence (*tme_split*). We found the best performance for the scheme *rnd_split*, reaching an R^2 of 0.77 and a root mean square error (RMSE) of 0.234 MPa; with the *tme_split*, the performance decreased to an R^2 of 0.62 and an RMSE of 0.36 MPa, both with XGBoost. The analysis of importance variables reveals that weather predictors, such as VPD, ET0, and temperature, have a higher weight in the model. These are followed by VIs that use short-wave infrared regions, which highlight the moisture stress index (MSI) and the disease and water stress index (DWSI). This model allows for precise monitoring of cherry water status, assists in optimizing the WUE, and can adapt to various climatic conditions.

1. Introduction

Climate change is increasingly recognized as a major driver of global water scarcity, exacerbating drought conditions and challenging water resources worldwide (Masson-Delmotte et al., 2021). This

phenomenon has heightened concerns about agricultural sustainability and food security (Molotoks et al., 2021), as the agricultural sector is particularly vulnerable to changes in precipitation patterns and rising temperatures (Fernández et al., 2023; Zambrano et al., 2016). In recent years, the central and northern regions of Chile have experienced severe reductions in water availability (Garreaud et al., 2017; Zambrano et al., 2024), with profound implications for agricultural productivity (Zambrano, 2023). The ongoing drought in Chile has intensified the need for efficient water use in agriculture (Zúñiga et al., 2021), particularly in fruit orchards, which are highly dependent on consistent and adequate irrigation to maintain productivity and quality (Liu et al., 2023; Vicente-Serrano et al., 2020). Efficient water management is thus crucial not only for reducing water consumption but also for optimizing plant health and maximizing yields under water-limited conditions (D'Odorico et al., 2020). This, in turn, aids in our adaptation to a changing climate where water resources are limited in certain areas.

To ensure efficient irrigation, the plant must replenish both the water lost through transpiration and the moisture removed from the soil by weather conditions, a process known as evapotranspiration (ET) (Allen et al., 1998). However, calculating ET in the field can be challenging. Two of the most precise methods are eddy covariance stations or water balances (Denager et al., 2020), which are costly and thus not used by the average farmer. In consequence, the ET is generally estimated by calculating the reference evapotranspiration (ET0), also known as atmospheric evaporative demand (Shirmohammadi-Aliakbarkhani and Saberali, 2020). ET0 can be roughly estimated from pan evaporation measuring the water loss, but the most common methods rely on meteorological data. The FAO Penman-Monteith method is recommended as the standard for calculating ET0 when sufficient weather data is available (Allen et al., 1998). When only temperature data is accessible, the Hargreaves-Samani method (Hargreaves and Samani, 1985) has shown good performance compared to the FAO Penman-Monteith method (Vicente-Serrano et al., 2007). Once the ET0 is calculated, it must be adjusted to ET by multiplying it by the crop coefficient (K_c), which varies depending on the crop type, growth stage, and condition, with tabulated values available (Allen et al., 1998). Despite their widespread use, these methods often lack spatial precision and may not account for variations in soil and plant water status across different orchard blocks, potentially leading to over- or under-irrigation (Jones, 2004). Furthermore, relying on generalized crop coefficients might not adequately capture the dynamic water needs of trees under varying environmental conditions, underscoring the need for more site-specific irrigation strategies.

To optimize irrigation, some studies have used regulated deficit irrigation (RDI), which consists of subjecting the plant to levels of water stress in different phenological stages (Yang et al., 2022). We can accomplish this by recovering by irrigation a portion of the ET that the plant has lost. To ensure good production and quality, irrigation typically recovers 100% of ET. Using RDI, we assess how the plan reacts physiologically and in terms of production and quality during specific phenological stages (Vélez-Sánchez et al., 2021). Alternatively, we could apply RDI and manage the irrigation based on the plant's response. For this, we can measure the plant's water potential (Corell et al., 2020). The water potential has been widely recognized as a reliable indicator of plant water status and a valuable tool for guiding irrigation decisions (Moriana et al., 2012; Naor, 2000). The solute concentration and water pressure in the leaf or stem directly show the water tension inside the plant, which is also called water potential. The water potential reflects the impact of soil water content, atmospheric water demand, and the plant's physiological responses (García-Tejera et al., 2021). Typically, we measure the water potential on the leaf, also known as the leaf water potential,

and on the stem, also known as the stem water potential. In the latter case, the leaf is put into a plastic bag and sealed with the aim that the leaf potential equilibrates with the water potential of the stem (Levin, 2019). The water potential usually is taken at different times during the day; when the measure is made around 12:00-14:00, it corresponds to midday stem water potential (Ψ_s). This range time corresponds to the maximum evaporative demand; thus, the Ψ_s tried to capture the water status of the plant at the highest stress time. This measurement has demonstrated consistency and reliability across various species (Carrasco-Benavides et al., 2022; Garofalo et al., 2023; Moriana et al., 2012). The Ψ_s vary during the season according to environmental factors and the irrigation applied, which reflected the plant water status. The major drawback of measuring Ψ_s, is that traditional methods, such as using a pressure chamber (Scholander et al., 1964), are labor-intensive, time-consuming, and not suitable for continuous monitoring or large-scale application (Jones, 2004).

New developments in remote sensing and modeling have made it possible to indirectly estimate Ψ_s by combining spectral and weather data with machine learning methods. This provides a scalable solution for managing irrigation in real time (Carrasco-Benavides et al., 2022; Garofalo et al., 2023; Savchik et al., 2024). Savchik et al. (2024) predicted Ψ_s in almond orchards, using ET, soil moisture, and spectral reflectance from unmanned aerial vehicles. They used the machine learning algorithms of random forests and neural networks. They reached R^2 values ranging from 0.33 to 0.73 and a root mean square error (RMSE) between 3.31 and 2.5 bars. In Italy, in an orchard of olives, Garofalo et al. (2023) uses random forests to estimate Ψ_s based on vegetation indices derived from spectral data from PlanetScope imagery, reaching an R^2 of 0.78, but when used to predict in an independent year, the results decreased significantly. Carrasco-Benavides et al. (2022) used infrared thermal imagery from unmanned aerial vehicles and derived the crop water stress index (CWSI). They used artificial neural networks to estimate Ψ_s in cherry-tree variety Regina. The test data produced a Pearson correlation value of 0.83, but the absence of independent selection may have inflated the values. These technologies provide the potential to enhance decision-making processes by enabling more precise and timely irrigation interventions based on the actual water needs of the crop. Remote sensing technologies have emerged as powerful tools for enhancing irrigation management by providing spatially detailed information on crop water status and variability across large areas (Zarco-Tejada et al., 2003). Sentinel-2 (S2), with its high spatial resolution and frequent revisit times, offers the ability to monitor vegetation by spectral indices, canopy cover, and thermal status, which are proxies of plant water stress (Addabbo et al., 2016; Jamshidi et al., 2021; Zhang et al., 2017). These indices, derived from multispectral imagery, can be used to assess crop water needs and optimize irrigation schedules more accurately than traditional methods. By integrating remote sensing data with weather and soil moisture measurements, it is possible to develop advanced irrigation management systems that respond dynamically to the actual water status of the crop, improving water use efficiency and crop performance (Baluja et al., 2012).

In this study, we aim to investigate the potential of using S2 and weather data to predict the daily spatial variation of Ψ_s in cherry orchards. To achieve this, we define three specific goals: i) to derive daily spatial predictors from S2 and weather stations; ii) to train and evaluate three machine learning models; and iii) to evaluate the spatio-temporal variation of estimated Ψ_s for monitoring irrigation. For this, we use satellite S2 (A/B) and weather data to derive multiple predictors. Then, we tested three machine learning algorithms: random forest (RF), extreme gradient boosting (XGBoost), and support vector machines (SVM). We use two splitting strategies, considering time and space, to obtain training and testing datasets. On the training dataset, we tune the model's parameters,

evaluate the models using resampling, and after that, we run them on the testing dataset. Finally, we use the best-performing model to estimate and evaluate the daily spatial variation of Ψ_s.

2. Materials and Methods

2.1. Study Area

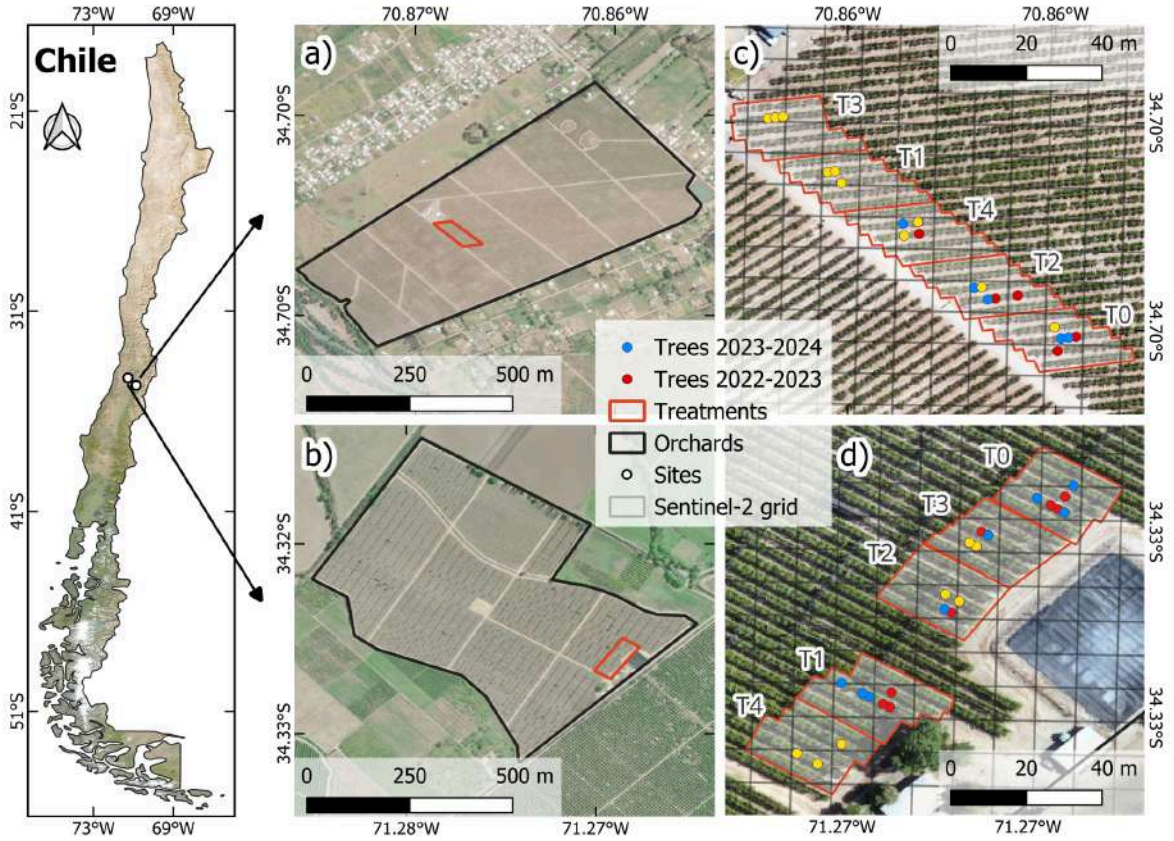

Figure 1. Study Area. The map on the left shows the orchards' location in Chile's central region. The maps on the right display the orchards in (a) Rio Claro and (b) La Esperanza, and (c) and (d) represent the irrigation treatments (T0, T1, T2, T3, T4). The red and blue dots represent the experimental trees selected for the 2022-2023 and 2023-2024 seasons, respectively, while the yellow dots indicate the trees selected for both seasons.

We conducted the study in two commercial orchards of sweet cherry trees (Prunus avium L., variety Regina) from the company Garces Fruit (www.garcesfruit.com) in the O'Higgins region of central Chile. The orchards are “Rio Claro,” having 60 ha and 9 year-olds, and “La Esperanza,” with 40 ha and 6 year-olds (Fig. 1a and 1b). The study took place during the irrigation seasons 2022–2023 and 2023–2024, which run from October to April. In Rio Claro, the soil has a sandy loam texture with low moisture retention, whereas in La Esperanza, the field is located on clayey soil with high moisture retention. For the two orchards in both seasons, full bloom occurred in October. The harvest in Rio Claro was on December 23rd, 2022, and January 3rd, 2024, and in La Esperanza on December 12th, for both seasons.

The climate of the region is mediterranean (Csb) (Beck et al., 2018) with moderate rainfall and an annual precipitation ranging from 200 to 500 mm/year in the last 10 years, concentrated in winter, with a prolonged dry season of 7 to 8 months (DMC, 2024). Each orchard has a private weather

station nearby, located 0.6 km from the center in Rio Claro and 1.4 km from the center in La Esperanza, respectively.

2.2. Deficit Irrigation

The local producer's irrigation in both orchards involves drip irrigation with two lines per row, operating from October to April (spring–summer) and halting during the winter dormancy period. In order to enhance the variability of plant water status, we implemented five different irrigation repositioning treatments in each orchard. To manage the irrigation amount, we used the ET0 and Ψ_s as references. Thus, we have T1, T2, T3, and T4 irrigation treatments, with T1 being the least restrictive and T4 the most restrictive regarding water supply (Fig. 1c and 1d). We also have a control treatment (T0) that receives standard irrigation from the local producer. Each treatment plot contained 60 trees and covered 0.048 ha. We applied the treatments during the consecutive growing seasons of 2022–2023 and 2023–2024, except that treatments T1 to T4 were not irrigated in La Esperanza during the 2023–2024 season, as the results from the previous season did not show any significant impact from the water restriction treatments. Table 1 shows the total volume of reference water demand (ET0), the total volume of water applied by the local producer in the control treatment (T0), and the total volume applied in deficit irrigation treatments, while Figure 2 illustrates the cumulative water depth (mm) for each treatment during irrigation, and the percentage relative to ET0.

Table 1. Total volume of reference evapotranspiration (ET0) and the volume of water applied in treatments for each orchard during the 2022-2023 and 2023-2024 seasons.

Treatment	Total volume of water (m^3/ha)			
	Rio Claro		La Esperanza	
	2022-2023	2023-2024	2022-2023	2023-2024
ET0	6,178	6,233	8,119	8,056
T0	5,128	4,066	3,840	3,740
T1	3,749	1,958	2,350	46
T2	2,937	1,333	1,504	25
T3	2,083	979	875	16
T4	1,312	625	456	46

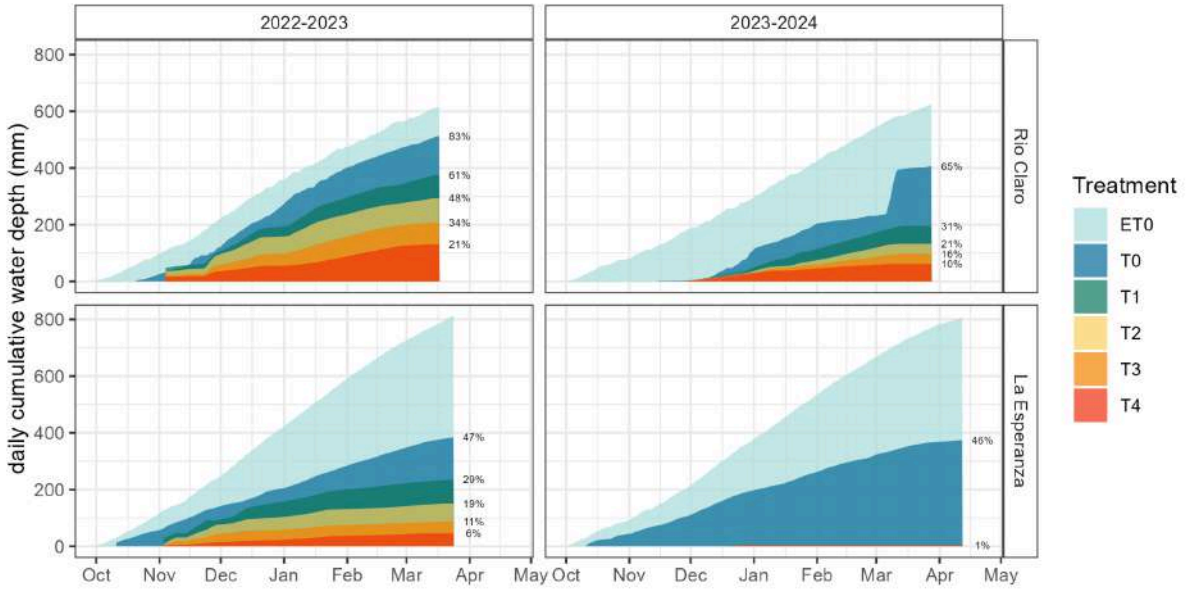

Figure 2. Variation of daily cumulative water depth (mm) applied by irrigation per treatment in comparison with reference evapotranspiration (ET0). The starting point for the accumulation of ET0 corresponds to the first day of irrigation for each orchard and season.

2.3. Data

2.3.1. In-situ midday stem water potential

Midday stem water potential (Ψ_s) was measured using a Scholander (Scholander et al., 1964) pressure chamber (Model 3000, Soil Moisture Equipment, Santa Barbara, CA, USA) connected to a nitrogen cylinder, following the procedures described by Turner (1981). Measurements were performed on mature leaves from the middle to the upper part of the tree on the north-facing side. We selected three trees per treatment in each orchard. One leaf per tree was sampled, totaling 15 measurements per orchard. In order to equilibrate the leaf water potential with the Ψs, leaves were wrapped in aluminum foil bags at least one hour before measurement. These measurements were conducted weekly between 12:00 and 14:00 h during both seasons, resulting in total measurement counts of 412 for Rio Claro (212 for 2022-2023; 200 for 2023-2024) and 486 for La Esperanza (176 for 2022-2023; 310 for 2023-2024).

2.3.2. Sentinel-2

S2 mission consists of two identical satellites, S2A and S2B, both equipped with a multispectral sensor featuring 13 spectral bands covering visible, near-infrared, and shortwave infrared regions, with spatial resolutions of 10, 20, and 60m (for technical specification see https://sentinels.copernicus.eu/en/web/sentinel/technical-guides/sentinel-2-msi). In this study, we utilized a total of 106 S2 (A/B) images, 54 for the 2022-2023 and 52 for the 2023-2024 season, captured between October and May in both orchards, tiles T19HCB for “La Esperanza” and T19HBB for “Río Claro”. The images were obtained from the atmospherically corrected S2 Level-2A collection from Planetary Computer (Microsoft Open Source et al., 2022), with a frequency of 5 days, at approximately 14:30 local time (UTC-4). A mask was applied based on the Scene Classification Layer (SCL) for values corresponding to “Cloud Shadows,” “Cloud Medium Probability,” and “Cloud High Probability,” respectively.

2.4. Deriving spatio-temporal predictors

2.4.1. In-situ weather variables

The automatic weather stations within both orchards recorded data on weather variables utilizing the ATMOS-41 model of METER group. These stations provided measurements of multiple meteorological variables every 15 minutes. We selected five meteorological variables that may affect water availability and plant physiological functionality: temperature (T°), relative humidity (RH), vapor pressure deficit (VPD), precipitation (PP), and reference evapotranspiration (ET0). We used these data to form the dataset for modeling (Fig. 3). We summed the precipitation and averaged the other variables daily.

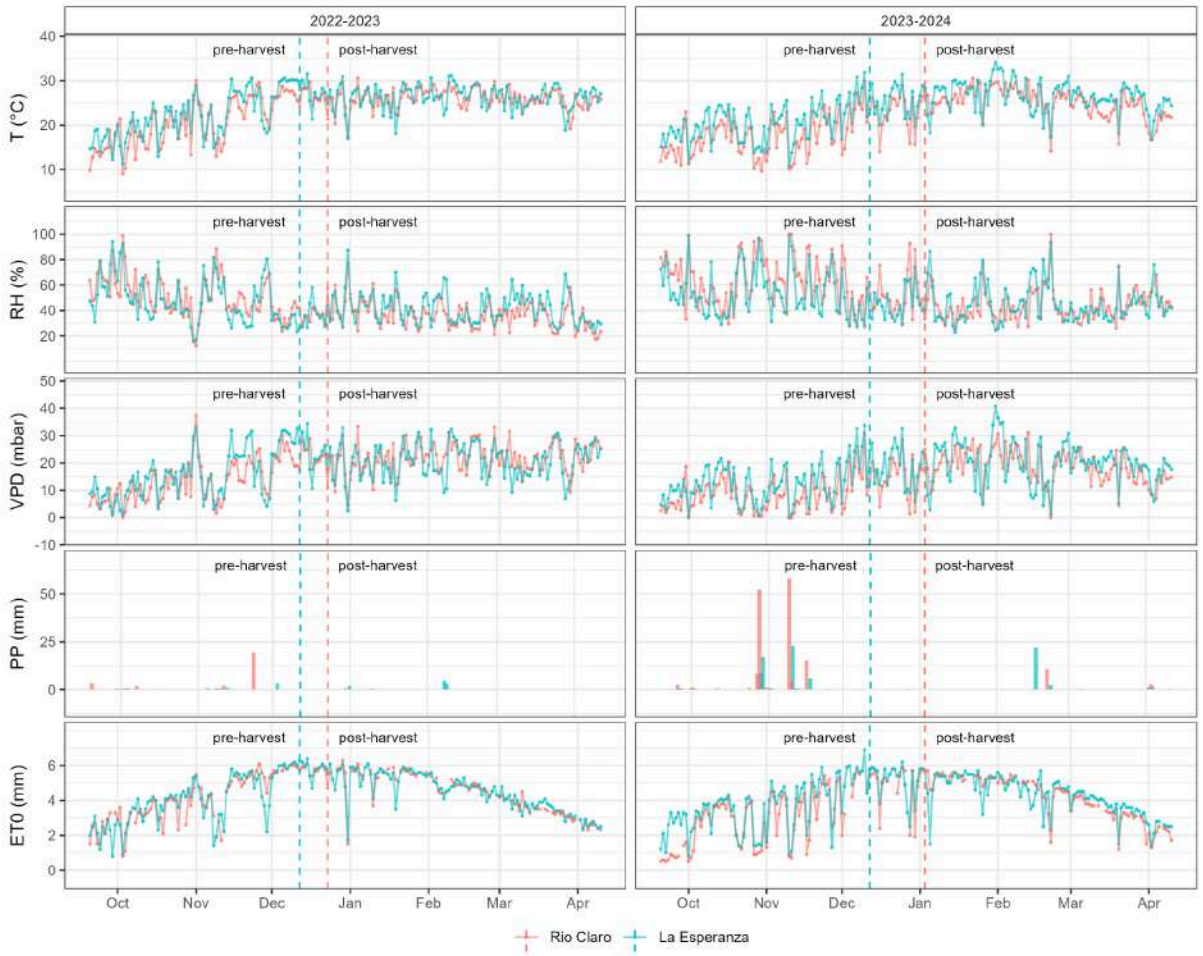

Figure 3. Time series of weather variables at the orchard sites *Rio Claro* and *La Esperanza* and the seasons 2022-2023 and 2023-2024. Vertical dashed lines indicate the harvest date for each orchard and season.

2.4.2. Vegetation indices derived from Sentinel-2

Sixteen VIs related to plant condition—vigor, stress, photosynthetic functionality, and water content—were derived from S2 data, as shown in Table 2. Nine indices do not include red-edge information, originating solely from the visible, NIR, and SWIR wavelength bands: NDVI, EVI, GCI, NDWI, NBR, NDMI, MSI, NMDI and DWSI. In contrast, seven indices—CLr, Clg, NDRE1, NDRE2, NDCI, mSR705, and RESI—were derived from red-edge information. The indices were calculated from the preprocessed images of S2 bands, obtaining time series for each VI across both orchards and seasons.

A smoothing process using local polynomial regression (LOESS) (Cleveland, 1979) model was applied to interpolate missing values (e.g., masked cause of cloudiness) between the Sentinel 5-day records. The LOESS method, which locally fits multiple regressions to the data using a weighted moving average, was implemented with a smoothing parameter (span) set to 0.3. As a result, a smooth, continuous daily predicted series for each index was obtained and then extracted for every measured tree. A correlation analysis was performed to evaluate the relationship between these smooth series and the observed Ψ_s. The Pearson correlation coefficient (r) was calculated across the trees for each day, orchard and season, and only daily significant correlations (p-value < 0.05) were used to compute a mean.

2.4.3. Biophysical parameters estimated from Sentinel-2

The Sentinel Application Platform (SNAP) is an integrated development environment (IDE) created by the European Space Agency (ESA, 2024) for analyzing and processing satellite data. SNAP provides a versatile suite of tools and functionalities for handling data from various Sentinel missions, including a biophysical parameter algorithm. This algorithm consists of two key components: (1) a radiative transfer model that inverts radiative properties from S2's multispectral imagery to retrieve vegetation parameters, and (2) a neural network model that further refines these parameters using empirical data. By applying these models and empirical relationships, SNAP extracts detailed information about the vegetation's physiological status (Weiss et al., 2020).

Using SNAP, we calculated various biophysical parameters, including LAI—leaf area index; FAPAR—fraction of absorbed photosynthetically active radiation; FVC—fraction of vegetation cover; CCC—canopy chlorophyll content; and CWC—canopy water content. These parameters were processed at 20 m for both seasons and orchard sites, and the same smoothing process used for the VIs was applied to fill gaps caused by missing data. The resulting biophysical parameters were used as predictors for modeling Ψ_s, along with the VIs and weather data (Table 2).

Table 2. Predictor variables for Ψ_s modeling. Weather variables from automatic stations (15 min frequency): T (°C), RH (%), VPD (mbar), PP (mm), ET0 (mm). Vegetation indices (VIs) derived from Sentinel-2 bands (10 m resolution) and biophysical parameters from SNAP (20 m resolution), both at 5-day intervals. B2 to B12 refer to Sentinel-2 MSI band reflectance.

Classification	Name	Description	Algorithm/Formula	Reference
Weather variables	T	Temperature		
	RH	Relative Humidity		
	VPD	Vapor Pressure Deficit	e^s-e^a (Eq.12 and Eq.14)	Allen et al. (1998)
	PP	Precipitation		
	ET0	Reference Evapotranspiration	FAO-Penman-Monteith	Allen et al. (1998)
Vegetation indices	NDVI	Normalized Difference Vegetation Index	$\frac{B8 - B4}{B8 + B4}$	Rouse et al. (1974)
	EVI	Enhanced Vegetation index	$\frac{2.5 \cdot (B8 - B4)}{(B8 + 6 \cdot B4 - 7.5 \cdot B2 + 1)}$	Huete et al. (2002)
	GCI	Green Coverage Index	$\frac{B9}{B3} - 1$	Gitelson et al. (2003)
	NBR	Normalized Burn Ratio	$\frac{B8 - B12}{B8 + B12}$	García and Caselles (1991)
	NDWI	Normalized Difference Water Index	$\frac{B3 - B8}{B3 + B8}$	McFeeters (1996)
	NDMI	Normalized Difference Moisture Index	$\frac{B8 - B11}{B8 + B11}$	Gao (1996)
	MSI	Moisture Stress Index	$\frac{B11}{B8}$	Huntjr and Rock (1989)
	NMDI	Normalized Multi-band Drought Index	$\frac{B8 - (B11 - B12)}{B8 + (B11 - B12)}$	Wang and Qu (2007)
	DWSI	Disease and Water Stress Index	$\frac{B8 + B3}{B11 + B4}$	Apan et al. (2004)
	CIr	Red Edge Chlorophyll	$\frac{B7}{B5} - 1$	Gitelson et al. (2003)
	CIg	Green Chlorophyll Index	$\frac{B7}{B3} - 1$	
	NDRE1	Normal Deviation Index of the Red Edge 1	$\frac{B6 - B5}{B6 + B5}$	Sims and Gamon (2002)
	NDRE2	Normal Deviation Index of the Red Edge 2	$\frac{B8 - B5}{B8 + B5}$	Barnes et al. (2000)
	NDCI	Normalized Difference Chlorophyll Index	$\frac{B5 - B4}{B5 + B4}$	Mishra and Mishra (2012)
	mSR705	Red Edge modified Simple Ratio	$\frac{(B6/B5) - 1}{\sqrt{(B6/B5) + 1}}$	Wu et al. (2008)
	RESI	Red Edge Spectral Index	$\frac{B7 + B6 - B5}{B7 + B6 + B5}$	Xiao et al. (2020)

Classification	Name	Description	Algorithm/Formula	Reference
Biophysical parameters	LAI	Leaf Area Index	PROSPECT + SAIL coupled model	Marie Weiss et al. (2020) Baret and Buis (2008)
	fAPAR	Fraction of Absorbed Photosynthetically Active Radiation		
	FVC	Fraction of Vegetation Cover		
	CCC	Canopy Chlorophyll Content		
	CWC	Canopy Water Content		

2.6. Modeling the daily spatial Ψ_s

2.6.1. Machine learning models (ML)

For Ψ_s modeling, we tested three machine learning algorithms (ML) : 1) Extreme Gradient Boosting (XGBoost; Chen and Guestrin (2016)); 2) Random Forest (RF; Ho (1995)); and 3) Support Vector Machine (SVM; Cortes and Vapnik (1995)). The first two methods utilize decision trees, while the later employs support vectors. These ML algorithms can be used for both classification and regression. We carried out a regression analysis, using the Ψ_s as the outcome and using 26 predictors: five of weather, 16 VIs, and five biophysical parameters (Table 2). We used 26 dates from seasons 2022–2023 and 34 from 2023–2024, totaling 60 dates. For each date, we take 30 measurements, 15 per orchard (Río Claro and La Esperanza). Thus, the complete dataset has 883 observations. For the modeling process, we proceed as follows: i) prepare and split the dataset into training and testing; ii) use the training dataset to adjust the algorithms' parameters by hyperparameter optimization; iii) resampling to account for reliability and recognize the most relevant variables to estimate Ψ_s, and iv) evaluate the model to gather the performance.

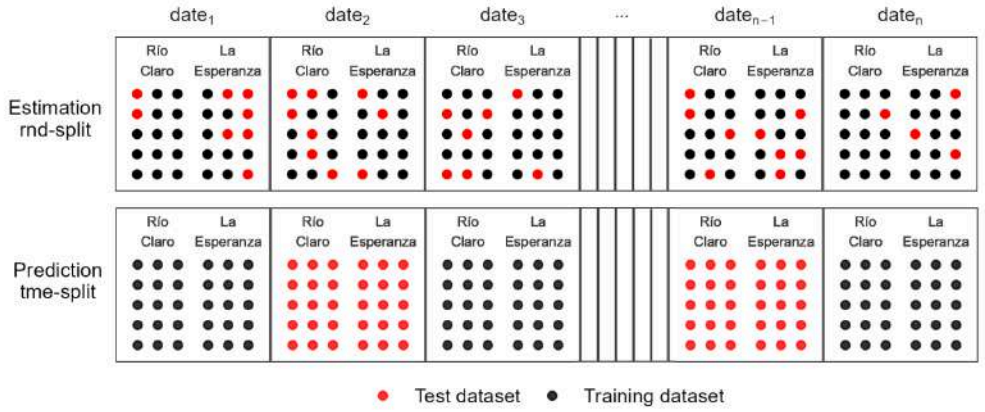

Figure 4. Split schemes used for grouping in training and testing datasets for the random split (rnd_split) and the independent time split (ind_split).

We trained the three models using two splitting schemes (Fig. 4), one in which we considered a random split taking testing and training data randomly (rnd_split) and a second one in which we used independent dates for training and testing (tme_split). We chose 75% of the data for training and 25% for testing in both cases. We used three types of feature engineering on the training data: i) we removed the predictors whose values remain constant by removing the zero-variance variables; ii) we normalized the predictors as they have a mean of zero and a standard deviation of one; and iii) we tested a model version that used partial least squares (PLS) (Wold, 1966) to cut down on the number of dimensions and used the five principal components as predictors. As a result, we used models with normalized predictors and others with the five principal components estimated by PLS.

To adjust the parameters of the models (XGBoost, RF, SVM) we used hyperparameter optimization. We start by setting each parameter's range (Table 3). We used five folds for resampling for both splitting schemes (*rnd_splt* and *tme_splt*). The hyperparameter optimization used a set of ten combinations of parameters per model. To evaluate the performance of the models, we used the metrics R^2, root mean square error (RMSE), and mean absolute error (MAE). Finally, we ranked the models based on the RMSE and R^2, selecting the models with the lowest RMSE and higher R^2.

Table 3. Range of initial values for the parameters adjusted in the tuning process for the models Extreme Gradient Boosting (XGBoost), Random Forest (RF), and Support Vector Machines (SVM).

Model	Parameter description	Identifier	Range
XGBoost and Random Forest	The number of trees contained in a random forest or boosted ensemble	trees	1000
	Number of randomly sampled predictors	mtry	1 - 28
	The minimum number of data points in a node that is required for the node to be split further	n_min	2 - 40
XGBoost	The maximum depth of the tree	tree_depth	1 - 15
	Learning rate	learn_rate	-3 - -0.5
	The reduction in the loss function required to split further	gamma	-10 - 1.5
	The size of the data set used for modeling within an iteration of the modeling algorithm	sample_size	0.1 - 1
Support Vector Machines	Regularization parameter	cost	-10 - 5
	Radial basis function sigma	rbf_sigma	-10 - 0

2.6.3. Evaluation and variable importance for the models

To evaluate the performance of the models, we used resampling over the training dataset for both splitting schemes (*rnd_split* and *tme_split*). We selected five folds, and calculated the metrics R^2, MAE, and RMSE for each fold.

To estimate the variable importance of each predictor on the model's performance, RF employs an out-of-bag permutation method in each tree, permuting over the predictors, and calculates the mean square error for each instance. For XGBoost, we estimate the fractional contribution of each feature to the model based on the total gain of the corresponding feature's splits. In the case of SVM, we compute permutation-based variable importance scores for the predictors (for more detail, see Greenwell and Boehmke (2020)).

2.7. Spatio-temporal variation of estimated Ψ_s

To estimate the daily spatial variation in the orchards of Rio Claro and La Esperanza, we selected the best-performing model from those generated with the random split (*rnd_split*) and evaluated it using resampling. This was done for all the days within each season. To analyze the spatial variation, we identified the days with the highest coefficient of variation. To assess the temporal variation we averaged the Ψ_s within each irrigation treatment and compared the difference between them for the two seasons. Also, using boxplot graphs, we compared the monthly distribution of values of Ψ_s for the five treatments.

2.8. Software

For downloading, processing, analyzing spatio-temporal data, and machine learning modeling, we used the R programming language for statistical computing and graphics (R Core Team, 2022). We used the data available in Planetary Computer (Microsoft Open Source et al., 2022), which we accessed via the {rstac} package (Simoes et al. (2021)). Preprocessing tasks, such as applying cloud coverage masks and cropping to the orchard plots, were performed using {gdalcubes} (Appel et al., 2021). For processing raster data, we used {terra} (Hijmans, 2024). To manage vectorial data, we used {sf} (Pebesma, 2018). For mapping, we used {tmap} (Tennekes, 2018). For data analysis and visualization, the suite {tidyverse} (Wickham et al., 2019) was used. For the machine learning modeling, we used the {tidymodels} (Kuhn and Wickham, 2020), {workflowsets} (Kuhn and Couch, 2024), {recipes} (Kuhn et al., 2024), {ranger} (Wright and Ziegler, 2017), {xgboost} (Chen et al., 2024), and {kernlab} (Karatzoglou et al., 2004) packages.

4. Results

4.1. Predictors and their relation to Ψs

4.1.2. Smoothing of Sentinel-2 derived indicators

Figure 4 shows the raw and smoothed-interpolated values of the most important satellite indicators in the model's performance for a random tree across both seasons and orchard sites. The values of the indices indicate variations in behavior throughout the various growing seasons. In both orchards, CCC, DWSI, mSR705, and NDMI increase during leaf expansion and higher water demand months (summer), peaking around or shortly after harvest dates between Jan-Mar and decreasing with leaf loss in Mar-Abr. In contrast, MSI exhibits opposite seasonal variability, reaching its lowest point after the harvest dates. NMDI shows unique behavior, with a tendency to decrease in the summer but with variable peaks throughout most months. The resulting series reveals a difference in magnitudes between the two orchards, with La Esperanza exhibiting higher values compared to Rio Claro (higher values for indices that increase in summer, and lower values for those that decrease during this period). Regarding both seasons, there are similarities in magnitude and variability, except for a sudden peak in La Esperanza during the second season between Jan-Mar and for NMDI in general.

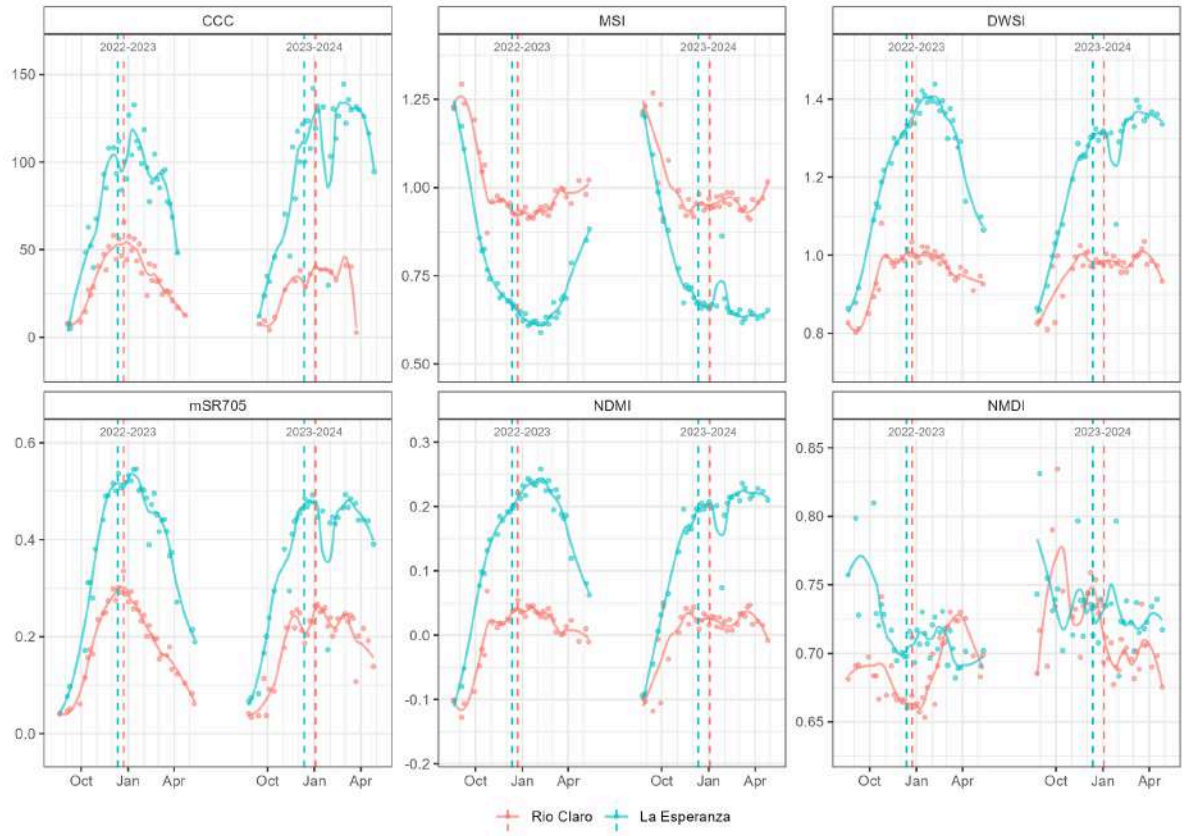

Figure 5. Time series of raw and smoothed-interpolated Sentinel-2 derived indicators most important to the model's performance at both orchard sites and seasons. Red points and lines correspond to Río Claro, while blue represents La Esperanza. Vertical dashed lines indicate the harvest dates for each orchard and season.

4.1.3. Correlation between predictors and Ψ_s

Table 4 presents the Pearson correlation coefficients between the daily mean values of each weather variable and the observed daily mean Ψ_s. The results indicate that ET0, VPD, and T are positively correlated with Ψ_s, while RH shows a negative correlation, and PP only exhibits weak correlations ranging between -0.1 and 0.1 for both sites during the 2022-2023 season. ET0 demonstrates a strong correlation ($r \geq 0.7$) at La Esperanza in both seasons, but not at Río Claro. In contrast, VPD, T, and RH generally exhibit strong correlations in most cases.

Table 4. Pearson correlation coefficient (r) between daily weather data and daily observed Ψ_s (-MPa).

Variable	Pearson correlation coefficient (r)			
	Rio Claro		La Esperanza	
	2022-2023	2023-2024	2022-2023	2023-2024
ET0	0.38	0	0.77	0.86
VPD	0.75	0.39	0.66	0.89
T	0.8	0.45	0.81	0.88
RH	-0.75	-0.43	-0.53	-0.83
PP	-0.11		0.1	

Regarding S2 derived predictors, Table 5 presents the mean of daily significant Pearson correlation coefficients (r; $p \leq 0.05$) between these predictors and the observed Ψ_s (MPa) for the 15 trees at both orchard sites and seasons. The results reflect differences between indices with positive and negative correlations, consistent with the seasonal behavior of these shown in Fig. 5. For CCC, DWSI,

mSR705, and NDMI, the mean correlations were positive and moderate (≥ 0.5) in all cases except for La Esperanza season 2023-2024, where CCC exhibited both positive and negative correlations on different days (Table 5). The same situation occurs with NMDI, which, along with MSI, averaged negative and moderate correlations (≤ -0.5) in all cases except for this specific group, where NMDI showed a positive correlation. Regarding the seasons, more significant correlations were found in the first season than in the second. In terms of orchards, more significant correlations were observed in Río Claro compared to La Esperanza.

Table 5. Mean of daily significant Pearson correlation coefficients (r) between Sentinel-2 derived predictors and observed Ψ_s (MPa) for the 15 trees across both orchard sites and seasons. n denotes the number of daily significant r obtained.

Orchard site	Season	Variable	r ± sd	n
Rio Claro	2022-2023	CCC	0.69 ± 0.11	5
		MSI	-0.66 ± 0.13	5
		DWSI	0.65 ± 0.12	4
		mSR705	0.69 ± 0.13	9
		NDMI	0.66 ± 0.13	5
		NMDI	-0.69 ± 0.1	6
	2023-2024	CCC	0.66 ± 0.01	2
		mSR705	0.63 ± 0.04	2
		NMDI	-0.55	1
La Esperanza	2022-2023	MSI	-0.59	1
		DWSI	0.61	1
		mSR705	0.52	1
		NDMI	0.59	1
	2023-2024	CCC*	0.03*± 0.88	2*
		NMDI	0.54	1

4.3. Modeling the daily spatial Ψs

4.3.1. Optimization of the parameter's models

4.3.2. Evaluation and variable importance of the models

Fig. 6 displays the R^2 ranking for each of the twelve different models trained with resampling (three algorithms, two splittings, and with or without partial least squares). Using the RMSE metric, the ranking behaves equally (see Fig. A1). With *rnd_split*, the R^2 range is 0.45 to 0.8, and with *tme_split*, it decreases to a range of 0.25 to 0.52. In the case of *rnd_split*, XGBoost and RF reached the highest R^2 with a mean of 0.77 and 0.76, respectively, followed by SVM with a R^2 of 0.68. On the *tme_split*, the R^2 difference between models is minor in comparison to those trained on the *rnd_split*. The three models that reached the maximum R^2 on *rnd_tme* are XGBoost, SVM, and pls_SVM (trained with the five principal components obtained from the partial least squares analysis as predictors), which are around 0.45. We selected the three models that reached the highest performance in the resampling evaluation per splitting scheme, hereafter named RF, XGBoost, and SVM.

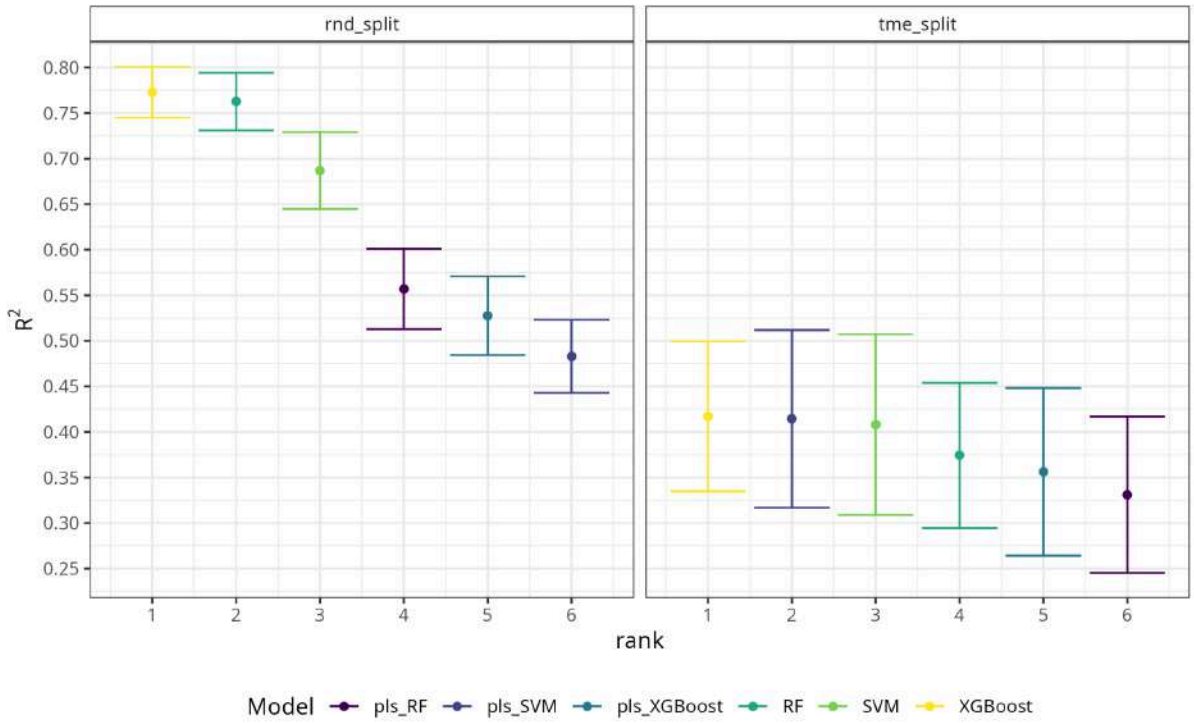

Figure 6. Ranking of machine learning models in the resampling according to the R^2 metric. The models are Random forest (RF), extreme gradient boosting (XGBoost), and support vector machines (SVM). The "pls" acronym beside the model name stands for partial least squares. Each panel corresponds to a splitting scheme: a random split (*rnd_split*) and a time-independent split (*tme_split*).

Fig. 7 shows the eleven most important variables in the model's performance. In the two splitting schemes, the meteorological data, specifically ET0, VPD, and temperature, hold the highest importance and reach their maximum weight. In SVM, RH is the only predictor in the *rnd_split*, and RH, VPD, and temperature are the predictors with higher importance in the *tme_split*. The S2-derived predictors came in second place after meteorological data. In the *rnd_split*, MSI, DWSI, mSR705, NDMI, and NMDI are the most relevant predictors for RF and XGBoost. When considering the *tme_split*, the MSI, DWSI, and NDMI are the most contributing variables to the model's performance. In the case of SVM model for *tme_split*, the biophysical parameter Cab holds the highest importance. As expected, the S2 predictors that were more closely related to Ψ_s were those using the SWIR wavelength, which is the spectral region more sensitive to water.

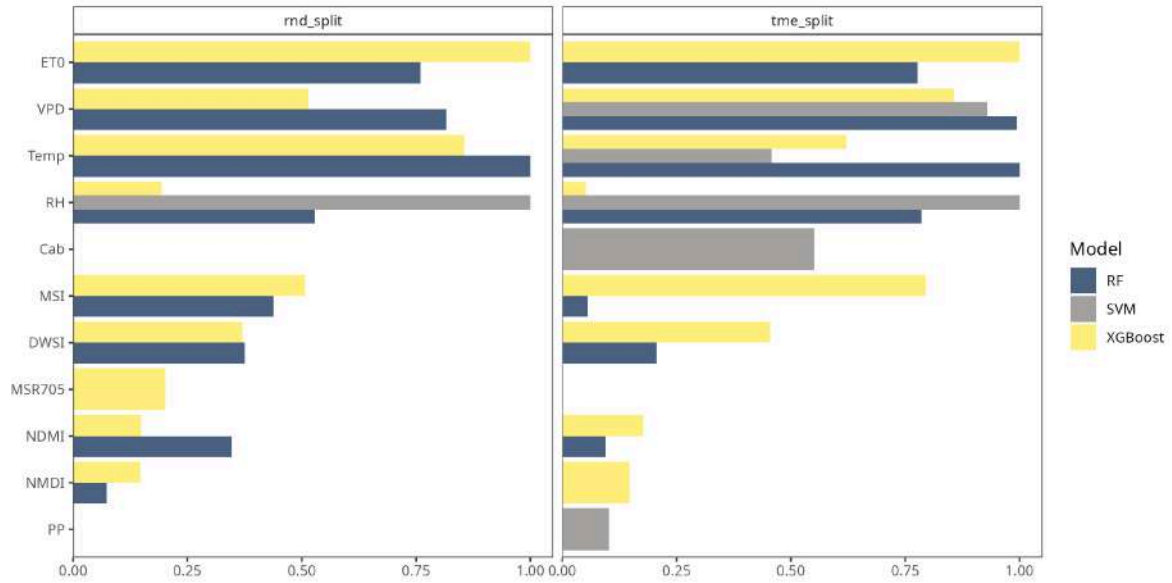

Figure 7. Variable importance is scaled (0–1) by machine learning models: random forest (RF), extreme gradient boosting (XGBoost), and support vector machines (SVM); for the two splitting schemes: random split (rnd_split) and time independent split (tme_split).

After the resampling evaluation, we trained the models on the testing dataset. In the *rnd_split*, the R^2 was 0.77, 0.76, and 0.63 for XGBoost, RF, and SVM, respectively (Fig. 8). The RMSE was between 2.34 MPa (XGboost) and 3.0 MPa (SVM). In the rnd_split, RF and XGBoost improve significantly over SVM. When trained in the tme_split, the model's performance decreases in comparison to those trained with rnd_split. Between them the models behave mostly equally, with an R^2 of 0.59 for RF and SVM and 0.62 for XGBoost. The RMSE was found to be between 0.33 MPa for XGBoost and 0.38 MPa for SVM. In Fig. 8, it can be seen that the error (observed minus estimated) increases for values lower than -1.5 MPa, corresponding to fewer points, thus the models do not have enough data to allow them to increase their performance. The reason for the lower data in this range is that it corresponds to higher water stress levels. Critical stress can lead to plant stomatal closure, which can impact both production and quality. The orchard owner did not recommend reaching this water stress level.

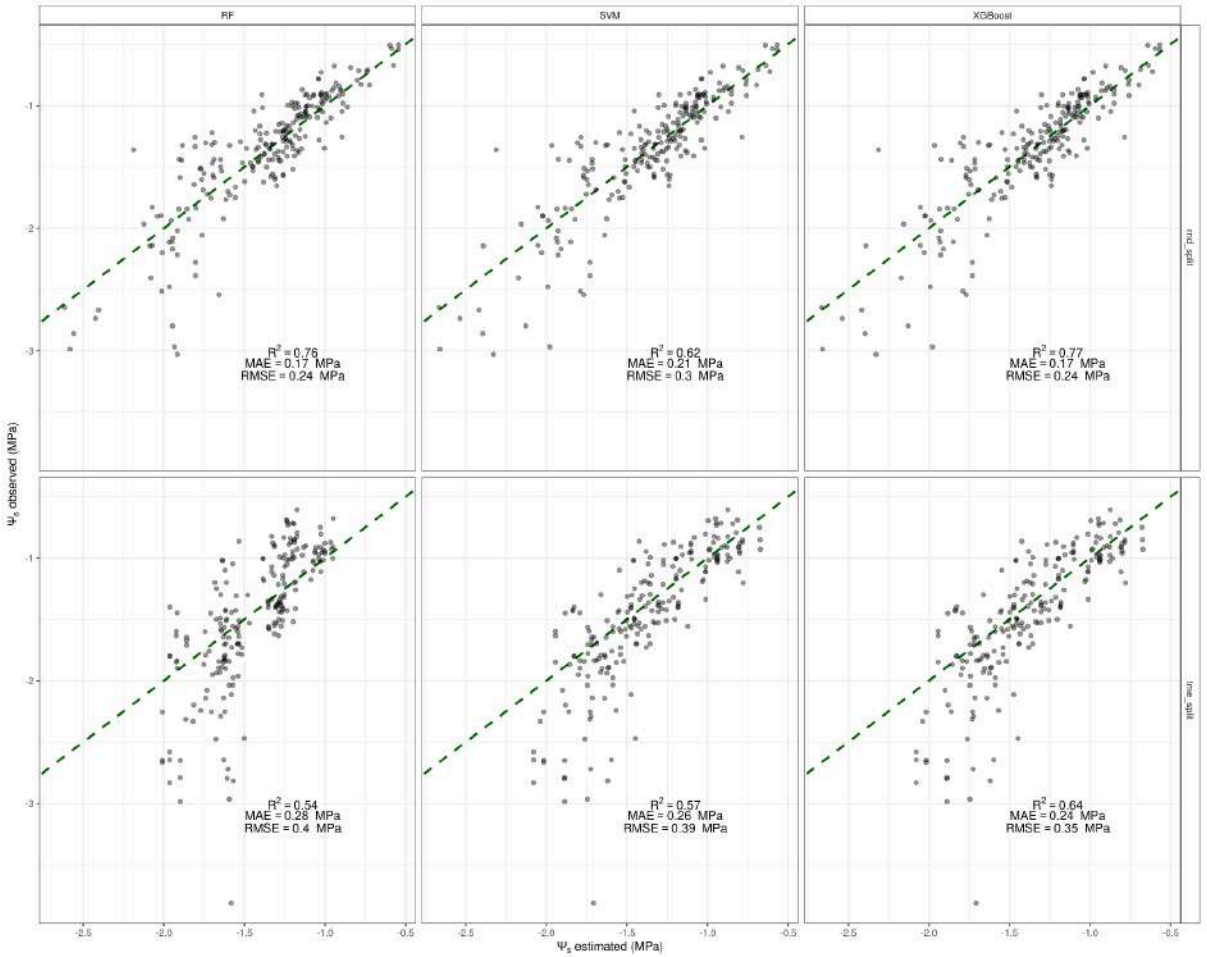

Figure 8. Predicted values into the testing dataset versus observed values of stem water potential (Ψs). The vertical panels correspond to the machine learning model: random forest (RF), extreme gradient boosting (XGBoost), and support vector machines (SVM). The horizontal panels correspond to the splitting schemes: random split (rnd_split) and time-independent split (tme_split). The metrics of performance used are r-squared (R^2), mean absolute error (MAE), and root mean squared error (RMSE).

4.4. Spatio-temporal variation of estimated Ψ_s

We used the XGBoost model trained over the *rnd_tme* (best-performing model) to estimate the daily spatial variation of Ψ_s over the orchard sites. Figs. 9 and 10 show the spatial variation of Ψ_s for the six dates that had the highest spatial variation (i.e., coefficient of variation) for the two orchard sites. The major spatial variation occurred in December and early January, corresponding to the higher water demand months (summer). The estimation of the whole orchard includes roads and infrastructure (see Fig. 1), which the model detects as the ones with lower Ψ_s. Despite that, the spatial estimation allows us to identify sectors with different plant water statuses. Figs. 9 and 10 show that in the Rio Claro orchard there is a higher spatial variation in comparison with La Esperanza. In Rio Claro, from the center to the north-east, a sector persists with lower pressures below -2 MPa. In La Esperanza, the response of Ψ_s is more uniform, with December 11th showing major spatial variation. However, given that this date coincides with harvest days, other factors such as the presence of people in the area could potentially influence the variation.

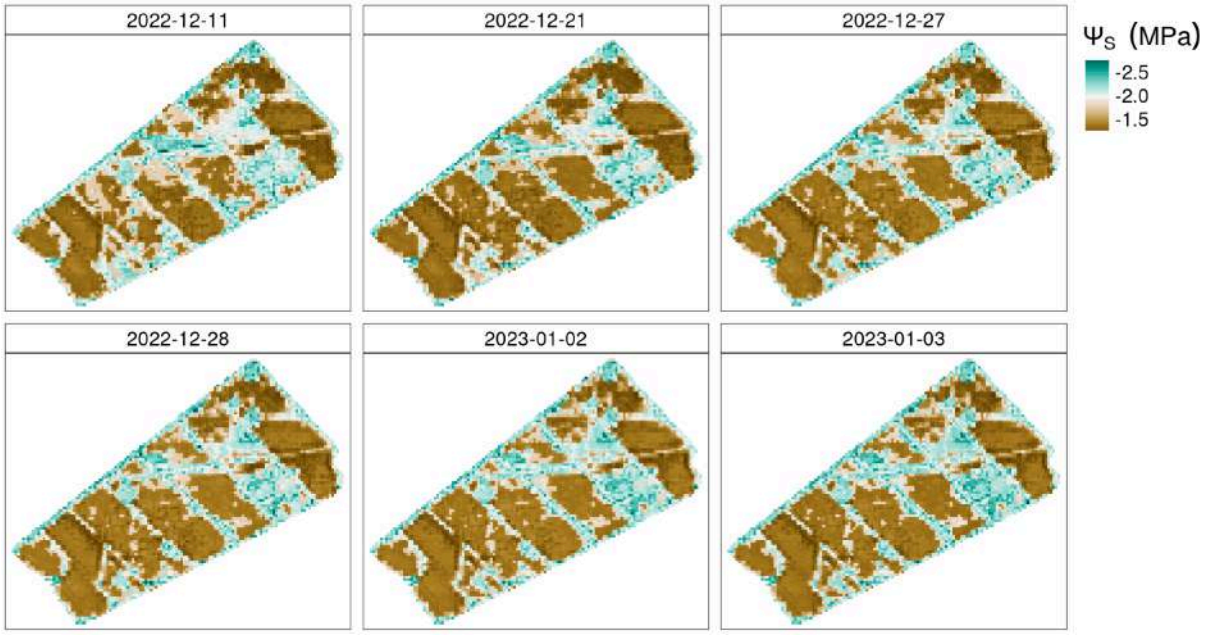

Figure 9. Midday stem water potential (Ψ_s) estimated by the extreme gradient boosting (XGBoost) model over the Río Claro orchard. The days selected correspond to the six with the maximum coefficient of variation.

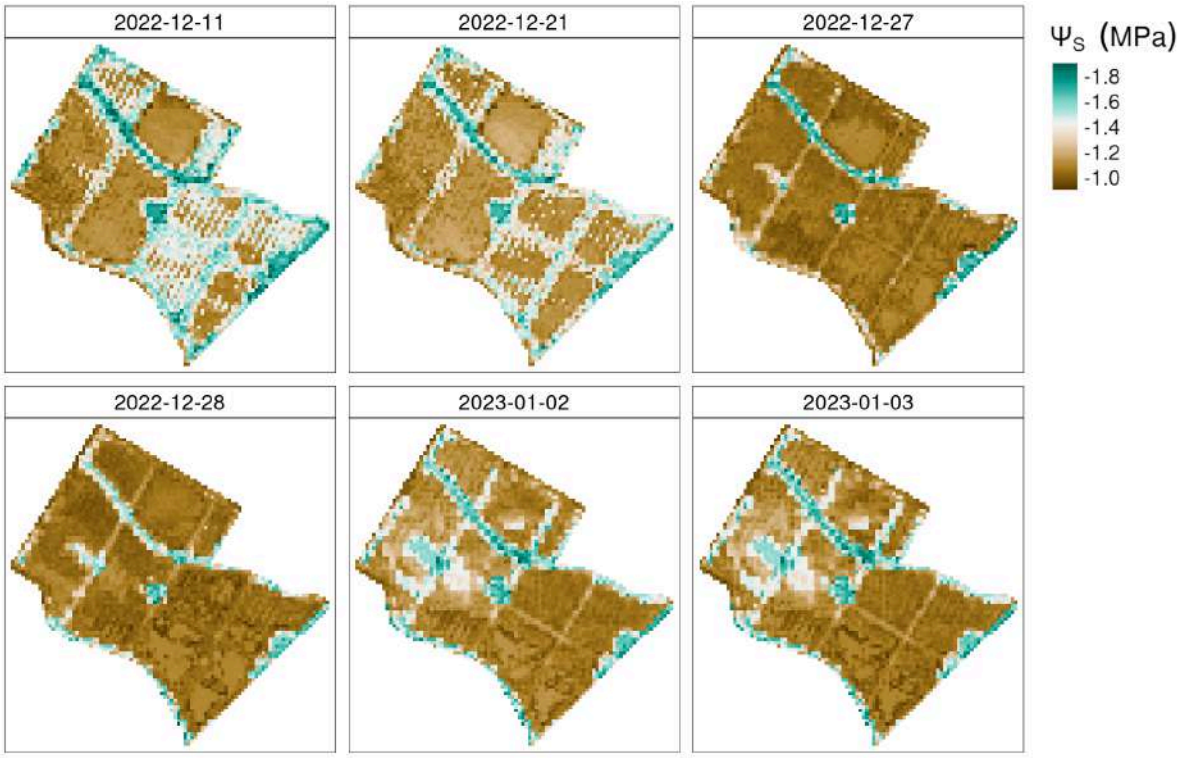

Figure 10. Midday stem water potential (Ψ_s) estimated by the extreme gradient boosting (XGBoost) model over the La Esperanza orchard. The days selected correspond to the six with the maximum coefficient of variation.

The averaged values of Ψ_s per treatment shown in Fig. 11 allow us to observe the temporal variation of the plant water status through the irrigation season (October to April) and the difference between treatments. The Ψ_s has been decreasing since October, reaching its lowest values between December and February, and then increasing until April, in line with the plant's water demand. For the two sites, the differences are most evident during the season 2022-2023 (Fig. 12), especially from

December to February. For 2023–2024, during November–December, the Ψ_s is higher in comparison to the previous season, this could be due to the precipitation fall during those months. The dispersion of values of Ψ_s is higher for October, November, and April, and it is tighter for the summer months (December–February) (Fig. 12). Additionally, the disparity between the various irrigation levels is more pronounced for the years 2022–2023, with a noticeable decrease in Ψ_s from T0 to T4, particularly in November and December.

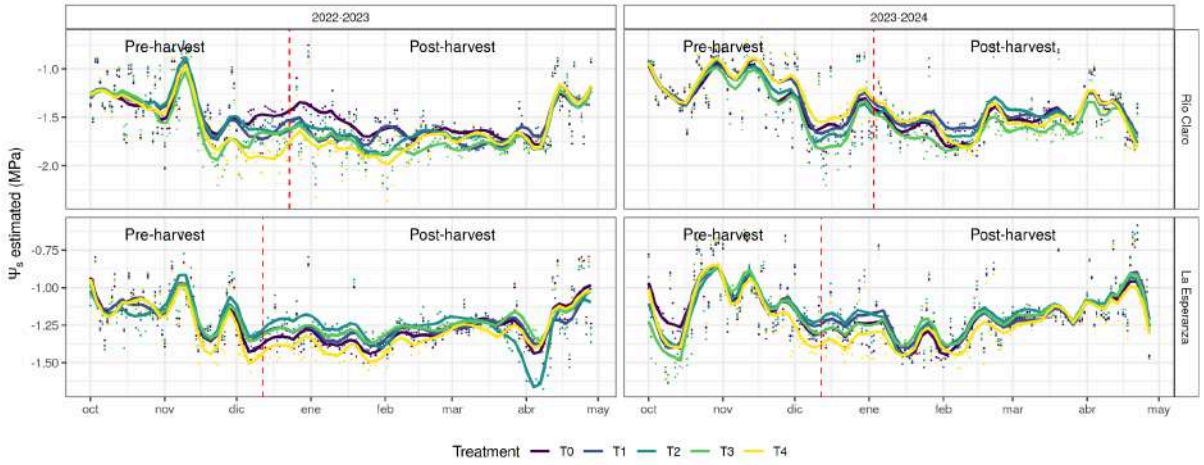

Figure 11. Averaged values of stem water potential (Ψ_s) estimated by the extreme gradient boosting model (XGBoost). The lines are the smoothed series for the five irrigation treatments, the seasons 2022-2023 and 2023-2024, as well as the orchards of Río Claro and La Esperanza.

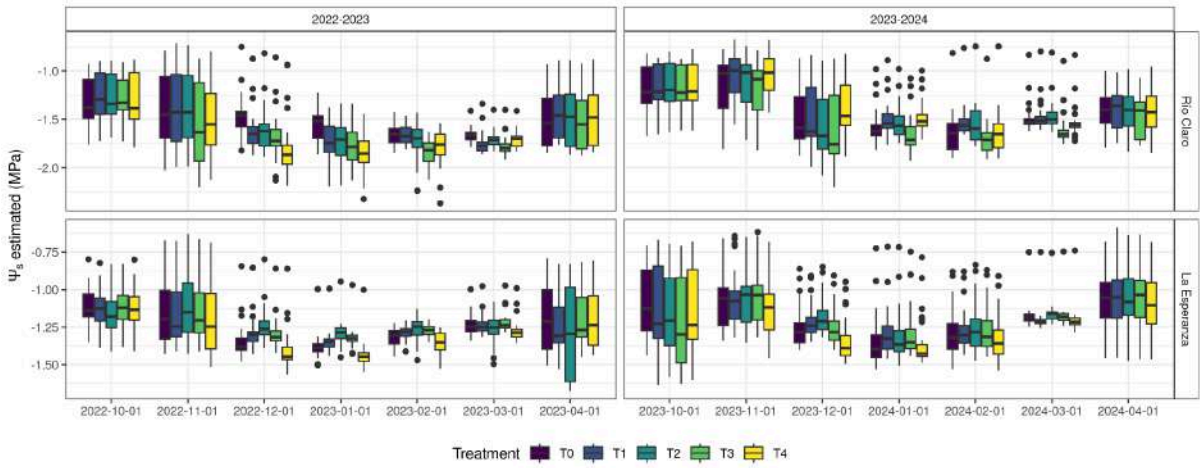

Figure 12. Distribution of daily values of estimated stem water potential (Ψ_s) by the extreme gradient boosting model (XGBoost) per month within the irrigation treatments for the seasons 2022-2023 and 2023-2024, as well as the orchards Río Claro and La Esperanza.

5. Discussion

5.1. Sources of uncertainty in the models

Some of the major sources of error in the model's prediction of the Ψ_s are the spatial resolution of the S2 images (10/20 meters), the temporal interpolation of vegetation predictors in between days of S2 revisit, and the null spatial representation of the weather data. The satellite passes over the

orchards near the time of the measurements, allowing for timely capture of the plant water status. However, one S2 pixel covers approximately 12 trees. Then, the cover area takes into account cherry canopy as well as background soil. Thus, the reflectance retrieved per pixel is a mixture of canopy and soil. This problem could be faced by spatial fusion techniques of S2 with high-resolution images (Dong et al., 2023; Galar et al., 2020) which will diminish the error due to this issue. Further, we used a simple low pass filter to interpolate daily values of vegetation predictors, which is a technique usually used for gap-filling in cloudy days (Mo et al., 2023), but not for interpolation. When assessing vegetation development, this technique may prove more beneficial as the physiological changes in development span more than a single day. However, the plant's water status changes on an hourly basis. A better approach to estimating daily values is the spatio-temporal fusion with Sentinel-3 (Wang and Atkinson, 2018) which takes into account the spectral reflectance. However, in this instance, a machine learning model utilizes all predictors, gathering temporal variation from weather data and spatial variability from S2 predictors. Therefore, the model functions effectively when the interpolated S2 predictors maintain the spatial variation associated with plant water status.

5.2. Sentinel-2 predictors most related to Ψ_s

The resulting S2 derived indices used as predictors for the model can be categorized based on their behavior between November and February, which corresponds to the period of rising temperatures, peak vegetative growth, and leaf expansion in cherry trees. Among the most significant of those affecting the model's performance, were DWSI, mSR705, and NDMI increasing during this period. Except for DWSI, these indices positively correlate with LAI, water and chlorophyll content in leaf and vegetation expansion (Gitelson et al., 2006; Wu et al., 2008; Gao 1996), while DWSI increases in summer due to higher temperatures and water stress (Apan et al. (2004)). In contrast, MSI and NMDI exhibit opposite seasonal variability. Some studies show that the MSI negatively correlates with Equivalent Water Thickness (EWT) and positively with LAI, increasing as LAI decreases and remaining lower during vegetative growth and leaf expansion (Huntjr and Rock, 1989). NMDI values rise in response to decreasing soil moisture during the leaf dormancy stage, while during foliar expansion, the values show minimal fluctuations according to variations in canopy water content (Wang and Qu, 2007).

Between the two seasons, we observe an extension of the peaks and troughs of the index values during the summer, indicating a prolongation of the period of vegetative growth and photosynthetic activity in the second season. Overall, the behavior of these indices suggests that in both Río Claro and La Esperanza, the trees are healthy, with high water and chlorophyll content and dense canopy cover. However, these conditions are more pronounced in La Esperanza compared to Río Claro. Between the two seasons, an extension of the peaks and troughs of the values is observed during the second season, indicating a delay in the productive season.

5.3. Comparison with other approaches

Numerous studies (Abrisqueta et al., 2015; Blanco et al., 2018) have correlated weather data, such as VPD, with plant water status in tree crops, achieving R^2 values of 0.72 and 0.88, making it a reliable indicator. The primary drawback is that stations that typically collect weather data lack spatial variation. Seamlessly, in our case, the VPD, ET0, and temperature were the predictors with a higher impact on the model's performance. The three predictors are interdependent, as VPD is dependent on temperature, and ET0 is also dependent on both VPD and temperature. To estimate the spatial variation of Ψ_s, one of the most used techniques is the use of UAS (Unmanned Air System) and thermal infrared imagery to derive the Crop Water Stress Index (CWSI). Thermal imagery (Alghory and Yazar, 2019; Blanco et al., 2023; Carrasco-Benavides et al., 2022; Park et al., 2021) offers a significant advantage due to its ability to capture high spatial resolution. Carrasco-Benavides et al. (2022) used the CWSI on cherry trees; they used neural networks and achieved a correlation coefficient of 0.83. Nevertheless, they used a random split for selecting the training and testing datasets; thus, their model allows estimation of Ψ_s but not prediction. Our model outperforms theirs, boasting an R^2 of 0.77 for estimation. Furthermore, the applicability of our methodology depends on remote data to run the model; in the case of CWSI models, it depends on the UAS unit and human staff to collect the imagery in the field, which makes a costly alternative.

6. Conclusion

The best-performing model to estimate and predict Ψ_s was the XGBoost algorithm. We used station weather variables and S2 satellite vegetation indicators as predictors. The model for estimation reached a high performance, having an R^2 = 0.77 and an RMSE = 0.234 MPa. The prediction model (*tme_split*) reduces the performance to R^2 = 0.62 and RMSE = 0.363 MPa. The weather variables VPD, ET0, and temperature were the most important predictors of temporal behavior, and the vegetation indices that measure in the SWIR region, MSI, DWSI, NMDI, and NDMI were the most important predictors of spatial variation.

The model provides an alternative to irrigation by utilizing evapotranspiration as a methodology to optimize irrigation in cherry orchards. More measurements of Ψ_s at higher plant water stress levels, both near and below stomatal closure, could enhance the model's effectiveness. Additionally, in future research, incorporating measurements on cloudy days could enhance the evaluation of performance on those days.

Acknowledgment

Chile's National Research and Development Agency (ANID) funded this study through the grants FONDEF IdEA I+D ID21I10297, the drought emergency FSEQ210022, Anillo ANID/ACT210007, and the FONDECYT 1230163 projects. We also thank the company Garces Fruit (https://garcesfruit.com/), which provides the orchards that allow us to carry out the study and offers expert advice and support throughout the research.

References

Abrisqueta, I., Conejero, W., Valdés-Vela, M., Vera, J., Ortuño, M.F., Ruiz-Sánchez, M.C., 2015. Stem water potential estimation of drip-irrigated early-maturing peach trees under Mediterranean conditions. Computers and Electronics in Agriculture 114, 7–13. https://doi.org/10.1016/j.compag.2015.03.004

Addabbo, P., Focareta, M., Marcuccio, S., Votto, C., Ullo, S.L., 2016. Contribution of Sentinel-2 data for applications in vegetation monitoring. ACTA IMEKO 5, 44. https://doi.org/10.21014/acta_imeko.v5i2.352

Alghory, A., Yazar, A., 2019. Evaluation of crop water stress index and leaf water potential for deficit irrigation management of sprinkler-irrigated wheat. Irrigation Science 37, 61–77. https://doi.org/10.1007/s00271-018-0603-y

Allen, R.G., Pereira, L.S., Raes, D., Smith, M., 1998. Crop evapotranspiration-guidelines for computing crop water requirements-fao irrigation and drainage paper 56. FAO, Rome.

Apan, A., Held, A., Phinn, S., Markley, J., 2004. Detecting sugarcane “orange rust” disease using EO-1 Hyperion hyperspectral imagery. International Journal of Remote Sensing 25, 489–498. https://doi.org/10.1080/01431160310001618031

Appel, M., Pebesma, E., Mohr, M., 2021. Cloud-based processing of satellite image collections in R using STAC, COGs, and on-demand data cubes.

Baluja, J., Diago, M.P., Balda, P., Zorer, R., Meggio, F., Morales, F., Tardaguila, J., 2012. Assessment of vineyard water status variability by thermal and multispectral imagery using an unmanned aerial vehicle (UAV). Irrigation Science 30, 511–522. https://doi.org/10.1007/s00271-012-0382-9

Baret, F., Buis, S., 2008. Estimating Canopy Characteristics from Remote Sensing Observations: Review of Methods and Associated Problems, in: Liang, S. (Ed.), Advances in Land Remote Sensing. Springer Netherlands, Dordrecht, pp. 173–201.

Barnes, E.M., Clarke, T.R., Richards, S.E., Colaizzi, P.D., Haberland, J., Kostrzewski, M., Waller, P., Choi, C., Riley, E., Thompson, T., Lascano, R.J., Li, H., Moran, M.S., 2000. COINCIDENT DETECTION OF CROP WATER STRESS, NITROGENSTATUS AND CANOPY DENSITY USING GROUND-BASEDMULTISPECTRAL DATA, in: Proceedings of the 5th International Conference on Precision Agriculture. Bloomington, Minnesota, EE. UU.

Beck, H.E., Zimmermann, N.E., McVicar, T.R., Vergopolan, N., Berg, A., Wood, E.F., 2018. Present and future Köppen-Geiger climate classification maps at 1-km resolution. Scientific data 5, 180214. https://doi.org/10.1038/sdata.2018.214

Blanco, V., Domingo, R., Pérez-Pastor, A., Blaya-Ros, P.J., Torres-Sánchez, R., 2018. Soil and plant water indicators for deficit irrigation management of field-grown sweet cherry trees. Agricultural Water Management 208, 83–94. https://doi.org/10.1016/j.agwat.2018.05.021

Blanco, V., Willsea, N., Campbell, T., Howe, O., Kalcsits, L., 2023. Combining thermal imaging and soil water content sensors to assess tree water status in pear trees. Frontiers in Plant Science 14, 1197437. https://doi.org/10.3389/fpls.2023.1197437

Carrasco-Benavides, M., Gonzalez Viejo, C., Tongson, E., Baffico-Hernández, A., Ávila-Sánchez, C., Mora, M., Fuentes, S., 2022. Water status estimation of cherry trees using infrared thermal imagery coupled with supervised machine learning modeling. Computers and Electronics in Agriculture 200, 107256. https://doi.org/10.1016/j.compag.2022.107256

Chen, T., Guestrin, C., 2016. XGBoost: A Scalable Tree Boosting System, in: Proceedings of the 22nd ACM SIGKDD International Conference on Knowledge Discovery and Data Mining. ACM, San Francisco California USA, pp. 785–794. https://doi.org/10.1145/2939672.2939785

Chen, T., He, T., Benesty, M., Khotilovich, V., Tang, Y., Cho, H., Chen, K., Mitchell, R., Cano, I., Zhou, T., Li, M., Xie, J., Lin, M., Geng, Y., Li, Y., Yuan, J., 2024. Xgboost: Extreme Gradient Boosting.

Cleveland, W.S., 1979. Robust Locally Weighted Regression and Smoothing Scatterplots. Journal of the American Statistical Association 74, 829–836.

Corell, M., Martín-Palomo, M.J., Girón, I., Andreu, L., Galindo, A., Centeno, A., Pérez-López, D., Moriana, A., 2020. Stem water potential-based regulated deficit irrigation scheduling for olive table trees. Agricultural Water Management 242, 106418. https://doi.org/10.1016/j.agwat.2020.106418

Cortes, C., Vapnik, V., 1995. Support-vector networks. Machine learning 20, 273–297.

D'Odorico, P., Chiarelli, D.D., Rosa, L., Bini, A., Zilberman, D., Rulli, M.C., 2020. The global value of water in agriculture. Proceedings of the National Academy of Sciences 117, 21985–21993. https://doi.org/10.1073/pnas.2005835117

Denager, T., Looms, M.C., Sonnenborg, T.O., Jensen, K.H., 2020. Comparison of evapotranspiration estimates using the water balance and the eddy covariance methods. Vadose Zone Journal 19, e20032. https://doi.org/10.1002/vzj2.20032

DMC, 2024. Portal de Servicios Climáticos.

Dong, R., Zhang, L., Li, W., Yuan, S., Gan, L., Zheng, J., Fu, H., Mou, L., Zhu, X.X., 2023. An adaptive image fusion method for Sentinel-2 images and high-resolution images with long-time intervals. International Journal of Applied Earth Observation and Geoinformation 121, 103381. https://doi.org/10.1016/j.jag.2023.103381

ESA, 2024. SNAP.

Fernández, F.J., Vásquez-Lavín, F., Ponce, R.D., Garreaud, R., Hernández, F., Link, O., Zambrano, F., Hanemann, M., 2023. The economics impacts of long-run droughts: Challenges, gaps, and way forward. Journal of Environmental Management 344, 118726. https://doi.org/10.1016/j.jenvman.2023.118726

Galar, M., Sesma, R., Ayala, C., Albizua, L., Aranda, C., 2020. Super-Resolution of Sentinel-2 Images Using Convolutional Neural Networks and Real Ground Truth Data. Remote Sensing 12, 2941. https://doi.org/10.3390/rs12182941

Gao, B., 1996. NDWI—A normalized difference water index for remote sensing of vegetation liquid water from space. Remote Sensing of Environment 58, 257–266. https://doi.org/10.1016/S0034-4257(96)00067-3

García, M.J.L., Caselles, V., 1991. Mapping burns and natural reforestation using thematic Mapper data. Geocarto International 6, 31–37. https://doi.org/10.1080/10106049109354290

García-Tejera, O., López-Bernal, Á., Orgaz, F., Testi, L., Villalobos, F.J., 2021. The pitfalls of water potential for irrigation scheduling. Agricultural Water Management 243, 106522. https://doi.org/10.1016/j.agwat.2020.106522

Garofalo, S.P., Giannico, V., Costanza, L., Alhajj Ali, S., Camposeo, S., Lopriore, G., Pedrero Salcedo, F., Vivaldi, G.A., 2023. Prediction of Stem Water Potential in Olive Orchards Using

High-Resolution Planet Satellite Images and Machine Learning Techniques. Agronomy 14, 1. https://doi.org/10.3390/agronomy14010001

Garreaud, R., Alvarez-Garreton, C., Barichivich, J., Boisier, J.P., Christie, D., Galleguillos, M., LeQuesne, C., McPhee, J., Zambrano-Bigiarini, M., 2017. The 2010-2015 mega drought in Central Chile: Impacts on regional hydroclimate and vegetation. Hydrology and Earth System Sciences Discussions 2017, 1–37. https://doi.org/10.5194/hess-2017-191

Gitelson, A.A., Gritz †, Y., Merzlyak, M.N., 2003. Relationships between leaf chlorophyll content and spectral reflectance and algorithms for non-destructive chlorophyll assessment in higher plant leaves. Journal of Plant Physiology 160, 271–282. https://doi.org/10.1078/0176-1617-00887

Gitelson, A.A., Merzlyak, M.N., Lichtenthaler, H.K., 1996. Detection of Red Edge Position and Chlorophyll Content by Reflectance Measurements Near 700 nm. Journal of Plant Physiology 148, 501–508. https://doi.org/10.1016/S0176-1617(96)80285-9

Greenwell, B.M., Boehmke, B.C., 2020. Variable Importance Plots—An Introduction to the vip Package. The R Journal 12, 343–366. https://doi.org/10.32614/RJ-2020-013

Hargreaves, G.L., Samani, Z.A., 1985. Reference crop evapotranspiration from temperature. Applied engineering in agriculture 1, 96–99.

Hijmans, R.J., 2024. Terra: Spatial Data Analysis.

Ho, T.K., 1995. Random decision forests, in: Proceedings of 3rd International Conference on Document Analysis and Recognition. IEEE, pp. 278–282.

Huete, A., Didan, K., Miura, T., Rodriguez, E.P., Gao, X., Ferreira, L.G., 2002. Overview of the radiometric and biophysical performance of the MODIS vegetation indices. Remote Sensing of Environment 83, 195–213. https://doi.org/10.1016/S0034-4257(02)00096-2

Huntjr, E., Rock, B., 1989. Detection of changes in leaf water content using Near- and Middle-Infrared reflectances☆. Remote Sensing of Environment 30, 43–54. https://doi.org/10.1016/0034-4257(89)90046-1

Jamshidi, S., Zand-Parsa, S., Niyogi, D., 2021. Assessing Crop Water Stress Index of Citrus Using In-Situ Measurements, Landsat, and Sentinel-2 Data. International Journal of Remote Sensing 42, 1893–1916. https://doi.org/10.1080/01431161.2020.1846224

Jones, H.G., 2004. Irrigation scheduling: Advantages and pitfalls of plant-based methods. Journal of Experimental Botany 55, 2427–2436. https://doi.org/10.1093/jxb/erh213

Karatzoglou, A., Smola, A., Hornik, K., Zeileis, A., 2004. Kernlab – An S4 Package for Kernel Methods in R. Journal of Statistical Software 11, 1–20. https://doi.org/10.18637/jss.v011.i09

Kuhn, M., Couch, S., 2024. Workflowsets: Create a Collection of 'tidymodels' Workflows.

Kuhn, M., Wickham, H., 2020. Tidymodels: A collection of packages for modeling and machine learning using tidyverse principles.

Kuhn, M., Wickham, H., Hvitfeldt, E., 2024. Recipes: Preprocessing and Feature Engineering Steps for Modeling.

Levin, A.D., 2019. Re-evaluating pressure chamber methods of water status determination in field-grown grapevine (Vitis spp.). Agricultural Water Management 221, 422–429. https://doi.org/10.1016/j.agwat.2019.03.026

Liu, X., Gao, T., Liu, C., Mao, K., Gong, X., Li, C., Ma, F., 2023. Fruit crops combating drought: Physiological responses and regulatory pathways. Plant Physiology 192, 1768–1784. https://doi.org/10.1093/plphys/kiad202

Masson-Delmotte, P.Z., V., L. Connors, S.B., C. Péan, R. Matthews, T.W., T. K. Maycock (Eds.), 2021. IPCC, 2021: Climate Change 2021: The Physical Science Basis. Contribution of Working Group I to the Sixth Assessment Report of the Intergovernmental Panel on Climate Change. Cambridge University Press. In Press.

McFeeters, S.K., 1996. The use of the Normalized Difference Water Index (NDWI) in the delineation of open water features. International Journal of Remote Sensing 17, 1425–1432. https://doi.org/10.1080/01431169608948714

Microsoft Open Source, McFarland, M., Emanuele, R., Morris, D., Augspurger, T., 2022. Microsoft/PlanetaryComputer: October 2022.

Mishra, S., Mishra, D.R., 2012. Normalized difference chlorophyll index: A novel model for remote estimation of chlorophyll-a concentration in turbid productive waters. Remote Sensing of Environment 117, 394–406. https://doi.org/10.1016/j.rse.2011.10.016

Mo, Y., Xu, Y., Liu, Y., Xin, Y., Zhu, S., 2023. Comparison of gap-filling methods for producing all-weather daily remotely sensed near-surface air temperature. Remote Sensing of Environment 296, 113732. https://doi.org/10.1016/j.rse.2023.113732

Molotoks, A., Smith, P., Dawson, T.P., 2021. Impacts of land use, population, and climate change on global food security. Food and Energy Security 10, e261. https://doi.org/10.1002/fes3.261

Moriana, A., Pérez-López, D., Prieto, M.H., Ramírez-Santa-Pau, M., Pérez-Rodriguez, J.M., 2012. Midday stem water potential as a useful tool for estimating irrigation requirements in olive trees. Agricultural Water Management 112, 43–54. https://doi.org/10.1016/j.agwat.2012.06.003

Naor, A., 2000. MIDDAY STEM WATER POTENTIAL AS A PLANT WATER STRESS INDICATOR FOR IRRIGATION SCHEDULING IN FRUIT TREES. Acta Horticulturae 447–454. https://doi.org/10.17660/ActaHortic.2000.537.52

Park, S., Ryu, D., Fuentes, S., Chung, H., O'Connell, M., Kim, J., 2021. Dependence of CWSI-Based Plant Water Stress Estimation with Diurnal Acquisition Times in a Nectarine Orchard. Remote Sensing 13, 2775. https://doi.org/10.3390/rs13142775

Pebesma, E., 2018. Simple Features for R: Standardized Support for Spatial Vector Data. The R Journal 10, 439–446. https://doi.org/10.32614/RJ-2018-009

R Core Team, 2022. R: A Language and Environment for Statistical Computing. R Foundation for Statistical Computing, Vienna, Austria.

Rouse, J., Haas, R.H., Scheel, J.A., Deering, D., 1974. Monitoring vegetation systems in the Great Plains with ERTS. Proceedings of the Third Earth Resources Technology Satellite- 1 Symposium 4, 301–317.

Savchik, P., Nocco, M., Kisekka, I., 2024. Mapping almond stem water potential using machine learning and multispectral imagery. Irrigation Science. https://doi.org/10.1007/s00271-024-00932-8

Scholander, P.F., Hammel, H.T., Hemmingsen, E.A., Bradstreet, E.D., 1964. Hydrostatic Pressure and Osmotic Potential in Leaves of Mangroves and Some Other Plants. Proceedings of the National Academy of Sciences 52, 119–125. https://doi.org/10.1073/pnas.52.1.119

Shirmohammadi-Aliakbarkhani, Z., Saberali, S.F., 2020. Evaluating of eight evapotranspiration estimation methods in arid regions of Iran. Agricultural Water Management 239, 106243. https://doi.org/10.1016/j.agwat.2020.106243

Simoes, R., De Souza, F.C., Zaglia, M., De Queiroz, G.R., Dos Santos, R.D.C., Ferreira, K.R., 2021. Rstac: An R Package to Access Spatiotemporal Asset Catalog Satellite Imagery, in: 2021 IEEE International Geoscience and Remote Sensing Symposium IGARSS. IEEE, Brussels, Belgium, pp. 7674–7677. https://doi.org/10.1109/IGARSS47720.2021.9553518

Sims, D.A., Gamon, J.A., 2002. Relationships between leaf pigment content and spectral reflectance across a wide range of species, leaf structures and developmental stages. Remote Sensing of Environment 81, 337–354. https://doi.org/10.1016/S0034-4257(02)00010-X

Tennekes, M., 2018. Tmap: Thematic Maps in R. Journal of Statistical Software 84, 1–39. https://doi.org/10.18637/jss.v084.i06

Turner, N.C., 1981. Techniques and experimental approaches for the measurement of plant water status. Plant and Soil 58, 339–366. https://doi.org/10.1007/BF02180062

Vélez-Sánchez, J.E., Balaguera-López, H.E., Alvarez-Herrera, J.G., 2021. Effect of regulated deficit irrigation (RDI) on the production and quality of pear Triunfo de Viena variety under tropical conditions. Scientia Horticulturae 278, 109880. https://doi.org/10.1016/j.scienta.2020.109880

Vicente-Serrano, S.M., Quiring, S.M., Peña-Gallardo, M., Yuan, S., Domínguez-Castro, F., 2020. A review of environmental droughts: Increased risk under global warming? Earth-Science Reviews 201, 102953. https://doi.org/10.1016/j.earscirev.2019.102953

Vicente-Serrano, S.M., Lanjeri, S., López-Moreno, J.I., 2007. Comparison of different procedures to map reference evapotranspiration using geographical information systems and regression-based techniques. International Journal of Climatology 27, 1103–1118. https://doi.org/10.1002/joc.1460

Wang, L., Qu, J.J., 2007. NMDI: A normalized multi-band drought index for monitoring soil and vegetation moisture with satellite remote sensing. Geophysical Research Letters 34, 2007GL031021. https://doi.org/10.1029/2007GL031021

Wang, Q., Atkinson, P.M., 2018. Spatio-temporal fusion for daily Sentinel-2 images. Remote Sensing of Environment 204, 31–42. https://doi.org/10.1016/j.rse.2017.10.046

Weiss, Marie, Baret, F., Jay, S., 2020. Sentinel2 ToolBox Level2 Products.

Weiss, M., Jacob, F., Duveiller, G., 2020. Remote sensing for agricultural applications: A meta-review. Remote Sensing of Environment 236, 111402. https://doi.org/10.1016/j.rse.2019.111402

Wickham, H., Averick, M., Bryan, J., Chang, W., McGowan, L.D., François, R., Grolemund, G., Hayes, A., Henry, L., Hester, J., Kuhn, M., Pedersen, T.L., Miller, E., Bache, S.M., Müller, K., Ooms, J., Robinson, D., Seidel, D.P., Spinu, V., Takahashi, K., Vaughan, D., Wilke, C., Woo, K., Yutani, H., 2019. Welcome to the tidyverse. Journal of Open Source Software 4, 1686. https://doi.org/10.21105/joss.01686

Wold, H., 1966. Estimation of principal components and related models by iterative least squares. Multivariate analysis 391–420.

Wright, M.N., Ziegler, A., 2017. Ranger: A Fast Implementation of Random Forests for High Dimensional Data in C++ and R. Journal of Statistical Software 77, 1–17. https://doi.org/10.18637/jss.v077.i01

Wu, C., Niu, Z., Tang, Q., Huang, W., 2008. Estimating chlorophyll content from hyperspectral vegetation indices: Modeling and validation. Agricultural and Forest Meteorology 148, 1230–1241. https://doi.org/10.1016/j.agrformet.2008.03.005

Xiao, C., Li, P., Feng, Z., Liu, Y., Zhang, X., 2020. Sentinel-2 red-edge spectral indices (RESI) suitability for mapping rubber boom in Luang Namtha Province, northern Lao PDR. International Journal of Applied Earth Observation and Geoinformation 93, 102176. https://doi.org/10.1016/j.jag.2020.102176

Yang, B., Fu, P., Lu, J., Ma, F., Sun, X., Fang, Y., 2022. Regulated deficit irrigation: An effective way to solve the shortage of agricultural water for horticulture. Stress Biology 2, 28. https://doi.org/10.1007/s44154-022-00050-5

Zambrano, F., 2023. Four decades of satellite data for agricultural drought monitoring throughout the growing season in Central Chile, in: Vijay P. Singh Deepak Jhajharia, R.M., Kumar, R. (Eds.), Integrated Drought Management, Two Volume Set. CRC Press, p. 28.

Zambrano, F., Lillo-Saavedra, M., Verbist, K., Lagos, O., 2016. Sixteen years of agricultural drought assessment of the biobío region in chile using a 250 m resolution vegetation condition index (VCI). Remote Sensing 8. https://doi.org/10.3390/rs8060530

Zambrano, F., Vrieling, A., Meza, F., Duran-Llacer, I., Fernández, F., Venegas-González, A., Raab, N., Craven, D., 2024. Shifts in water supply and demand drive land cover change across Chile. https://doi.org/10.31223/X5CD80

Zarco-Tejada, P.J., Rueda, C.A., Ustin, S.L., 2003. Water content estimation in vegetation with MODIS reflectance data and model inversion methods. Remote Sensing of Environment 85, 109–124. https://doi.org/10.1016/S0034-4257(02)00197-9

Zhang, T., Su, J., Liu, C., Chen, W.-H., Liu, H., Liu, G., 2017. Band selection in sentinel-2 satellite for agriculture applications, in: 2017 23rd International Conference on Automation and Computing (ICAC). IEEE, Huddersfield, United Kingdom, pp. 1–6. https://doi.org/10.23919/IConAC.2017.8081990

Zúñiga, F., Jaime, M., Salazar, C., 2021. Crop farming adaptation to droughts in small-scale dryland agriculture in Chile. Water Resources and Economics 34, 100176. https://doi.org/10.1016/j.wre.2021.100176

Anexos

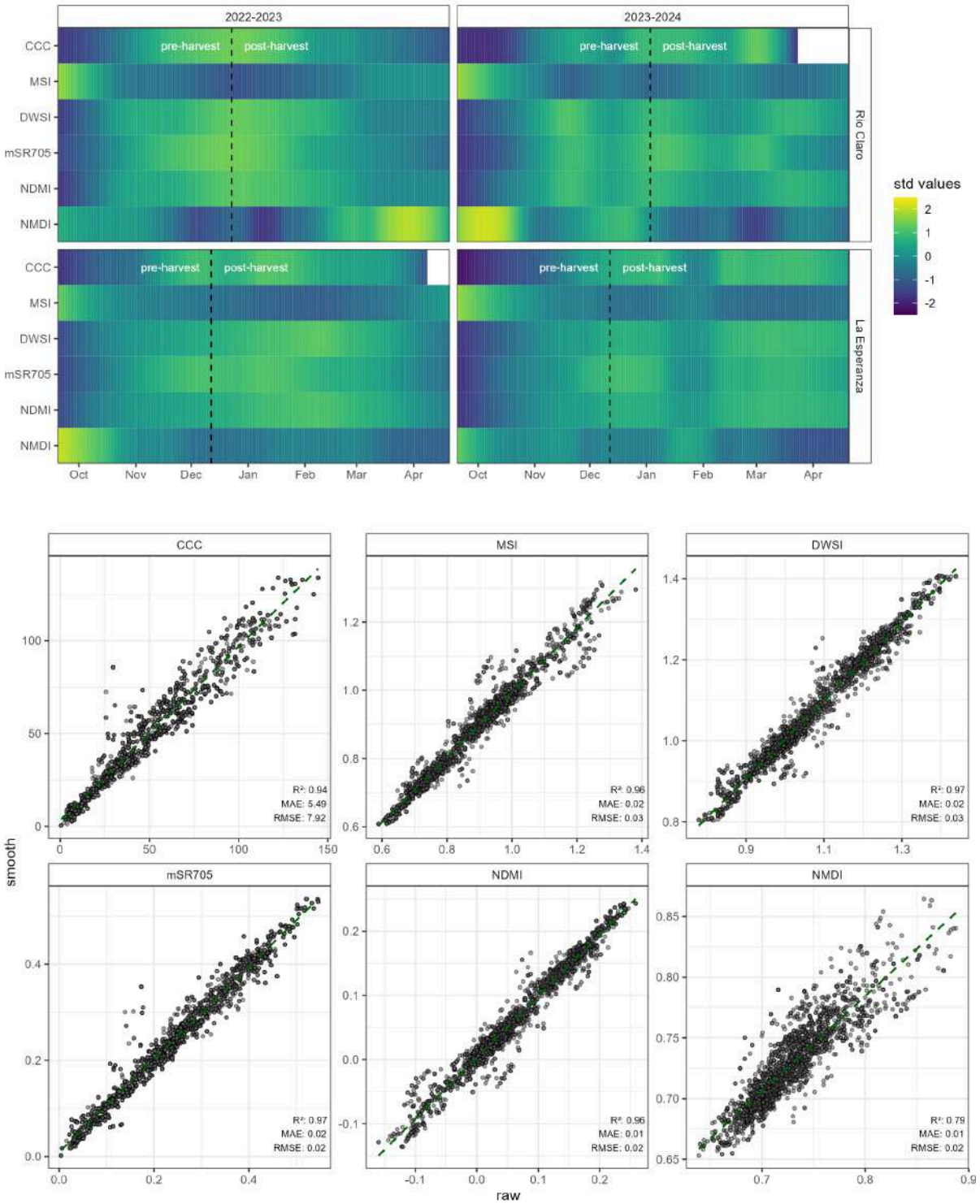

Appendix X. Scatterplots of raw vs. smoothed Sentinel-2 derived predictors most important for model performance and metrics. The green dashed line indicates the 1:1 line.

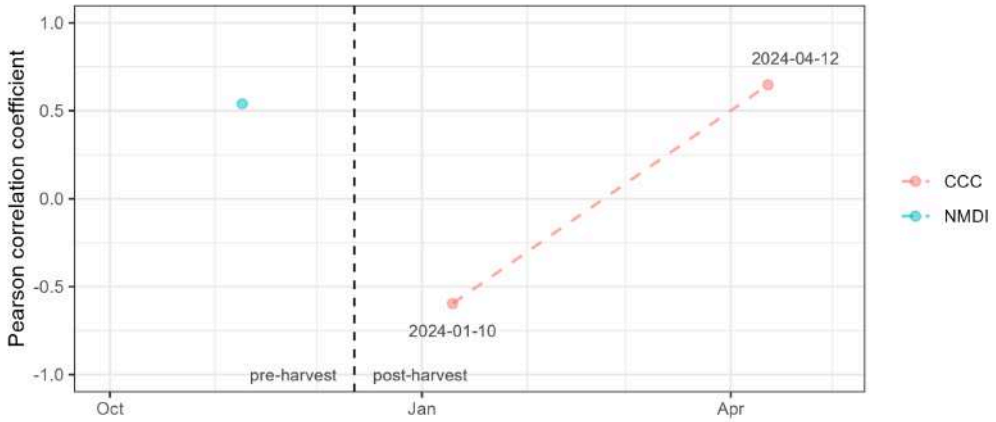

Appendix X. Daily significant Pearson correlation coefficient between CCC—NMDI and observed Ψ_s in La Esperanza season 2023-2024. Dashed black line represents the harvest date in the orchard.

Appendix X. Band information of the Sentinel-2 multispectral instrument (MSI) sensor. Bands used are marked (*).

Band	Sentinel-2A		Sentinel-2B		Resolution (m)
	Central Wavelength (nm)	Bandwidth (nm)	Central Wavelength (nm)	Bandwidth (nm)	
Band 1: Coastal aerosol	442.7	20	442.3	20	60
Band 2: Blue	492.7	65	492.3	65	10
Band 3: Green	559.8	35	558.9	35	10
Band 4: Red	664.6	30	664.9	31	10
Band 5: Vegetation Red Edge 1	704.1	14	703.8	15	20
Band 6: Vegetation Red Edge 2	740.5	14	739.1	13	20
Band 7: Vegetation Red Edge 3	782.8	19	779.7	19	20
Band 8: NIR	832.8	105	832.9	104	10
Band 8A: Vegetation Red Edge	864.7	21	864.0	21	20
Band 9: Water Vapor	945.1	19	943.2	20	60
Band 10: SWIR - Cirrus	1373.5	29	1376.9	29	60
Band 11: SWIR 1	1613.7	90	1610.4	94	20
Band 12: SWIR 2	2202.4	174	2185.7	184	20